Iranian Journal of Materials Forming 12 (4) (2025) 20-33

Online ISSN: 2383-0042

Iranian Journal of Materials Forming

Journal Homepage: http://ijmf.shirazu.ac.ir

Research Article

Hot Deformation Behavior of an API X70 Steel: A Processing Map Approach

Fatemeh Ahmadi, Mohsen Reihanian, Mostafa Eskandari* and Seyed Reza Alavi Zaree

Department of Materials Science and Engineering, Faculty of Engineering, Shahid Chamran University of Ahvaz, Ahvaz, Iran

ARTICLE INFO

Article history:

Received: 1 August 2025
Reviewed: 25 August 2025
Revised: 30 August 2025
Accepted: 31 August 2025

Keywords:

API X70 steel
Hot deformation
Processing map
Microstructure

Please cite this article as:

Ahmadi, F., Reihanian, M., Eskandari, M., & Alavi Zaree, S. R. (2025). Hot deformation behavior of an API X70 steel: A processing map approach. *Iranian Journal of Materials Forming*, *12*(4), 20-33. https://doi.org/10.22099/IJMF.2025.53864.1341

ABSTRACT

The hot deformation behavior of API X70 microalloyed steel was investigated using a processing map approach. Cylindrical specimens were compressed at temperatures of 950–1100 °C and strain rates of 0.001–1 s^{-1}. The flow curves exhibited typical features of work hardening, dynamic recovery, and dynamic recrystallization. Power dissipation efficiency and instability criteria were evaluated using the dynamic materials model to construct processing maps at various strain levels. At higher strains, three optimal hot deformation regions were identified, with the most favorable zone (25–33% efficiency) located at 1075–1100 °C and 0.001–0.005 s^{-1}. Microstructural validation confirmed these safe regions, while unstable domains were characterized by crack formation and deformation bands. Constitutive analysis determined an apparent activation energy of 572.5 kJ/mol. These findings provide practical guidance for optimizing the hot working parameters of API X70 steel.

1. Introduction

The steel industry plays a pivotal role in modern society, supplying essential materials for diverse applications [1]. Among these, high grade API steel is distinguished by its exceptional strength and toughness, making it a preferred material for critical structures such as pipelines and offshore platforms [2]. To optimize the processing of this steel and ensure desirable mechanical properties, a thorough understanding of its hot deformation behavior is crucial. Hot deformation, the process of plastically deforming metals at elevated temperatures, enables controlled shaping and microstructure modification, which ultimately determine the final properties of the material [3]. However, the hot deformation behavior of API steels is complex, being strongly influenced by deformation temperature, strain rate, and initial microstructure [4]. Numerous studies have examined the influence of these parameters on the microstructure, texture, and mechanical properties of API X70 steel, a significant and commonly utilized

---

* Corresponding author
E-mail address: m.eskandari1362@gmail.com (M. Eskandari)
https://doi.org/10.22099/IJMF.2025.53864.1341

variety of API steel. Reported findings highlight the formation of distinct microstructures and textures under different processing routes [5-7], as well as the roles of deformation temperature, strain rate, and reheating/finish rolling temperatures in recrystallization and their link to tensile properties [8, 9].

Despite the extensive body of work, a systematic investigation the hot deformation behavior of X70 steel using the processing map remains limited. This technique, based on hot compression testing across a wide range of temperatures and strain rates, provides valuable insights into optimal processing conditions for achieving desirable microstructures and mechanical properties [10], while also identifying microstructure evolution, flow stress, and potential instability regions during deformation [11].

The present study addresses this gap by comprehensively analyzing the hot deformation behavior of API X70 steel through the processing map approach. While various approaches are employed for the construction of processing maps, the current work utilizes the classical approach [12]. By conducting a series of hot compression tests and analyzing the resulting data, the work identifies the optimal processing windows for this steel, providing valuable guidance for its manufacturing and processing. Furthermore, the activation energy for hot deformation was determined, offering further insights into the material's thermal workability. The findings are expected to provide practical guidelines for hot working, thereby enhancing both the formability and mechanical performance of X70 pipeline steel.

2. Materials and Methods

2.1. Compression testing and materials preparation

The study used cylindrical compression specimens (length-to-diameter ratio of 1.4) machined from X70 steel sheets. The chemical composition (wt.%) is listed in Table 1.

The specimens were homogenized at 1200 °C for 10 minutes, quenched in water, and then subjected to compression tests (up to strain of 0.7) at various temperatures (950–1100 °C) and initial strain rates (0.001–1 s^{-1}). The cylindrical samples measured 10 mm in height and 7 mm in diameter and were prepared from rolled plates of X70 API steel. Compression testing was conducted using a Zwick Z250 machine, with a maximum load capacity of 250 kN. Graphite sheets were applied to minimize friction. The reported strain rates correspond to initial values to avoid crosshead speed effects, and, given the small specimen size and test temperatures; adiabatic heating was considered negligible under the present conditions.

All hot compression tests were carried out from a fully austenitic condition after reheating to the test temperature. Consequently, the room-temperature phases present after homogenization and quenching were not the operative starting microstructure during deformation; their influence was indirect, through segregation reduction, precipitate conditioning, and the austenite grain size established upon reheating.

The hot compression tests were performed once for each specified combination of temperature and strain rate due to the extensive time and resource requirements of the experiments. To ensure the reliability of the derived data and subsequent analyses, efficiency and instability criteria were calculated at different strain levels, and the corresponding processing maps were plotted. The validity of the processing maps was rigorously confirmed through microstructural characterization of samples deformed under both predicted stable and unstable conditions. This microstructural validation served as a direct form of experimental evidence, corroborating the theoretical predictions of the processing maps and providing confidence in the identified optimal and unstable deformation zones. To characterize microstructural changes, selected samples were sectioned, mounted, polished, and etched (Nital 2%) for optical microscopy. A 4% Picral solution was also employed to reveal the prior austenite grain boundaries.

Table 1. Chemical composition (wt.%) of the steel used in this study

Fe	C	Mn	Si	P	S	Cr	Mo	Ni	V	W	Cu	Al	Nb	Ti	B	Ca
Bal.	0.082	1.45	0.26	0.013	0.002	0.015	0.078	0.12	0.035	0.02	0.021	0.039	0.042	0.016	0.0005	0.002

2.2. Dynamic material modeling

The total power (*P*) dissipated during deformation process can be divided into two components: *G*, the power dissipated due to plastic deformation and *J*, the power dissipated due to microstructural evolution. The efficiency of power dissipation (η) is determined by [13]:

$$\eta = \frac{J}{J_{max}} = \frac{2m}{m+1} \tag{1}$$

Where *m* is the strain rate sensitivity. The factor *m* can be used to estimate the value of *J* at a specific temperature and strain rate using Eq. (1). The workpiece serves as a linear dissipator, and the value of *J* reaches its maximum (J_{max}) at $m = 1$. A power dissipation map can therefore be constructed by plotting contours of η based on deformation strain rate and temperature.

Various instability criteria have been proposed for constructing processing maps for different alloys, including superalloy GH4742 [14] and Ti-IF steel [15]. Among the most widely used are the criteria developed by Murty [16] and Prasad [10, 13]. Murty's instability criterion is versatile as it can be applied to any stress and strain rate curve, and it is based on the definitions of the power strain rate sensitivity (*m*) and efficiency (η) as follows [16]:

$$2m < \eta \tag{2}$$

For the present study, we utilized Prasad's instability criterion. This criterion, based on irreversible thermodynamics, is highly effective in identifying regions of flow instability, as defined below [10, 13]:

$$\xi(\dot{\varepsilon}) = \frac{\partial \ln\left(\frac{m}{m+1}\right)}{\partial \ln(\dot{\varepsilon})} + m < 0 \tag{3}$$

The strain rate sensitivity and strain rate can be used to calculate the instability parameter (ξ). If ξ is negative, the material is prone to instability. By combining the power dissipation map with the instability map, a processing map can be generated. This map provides valuable insights into optimal deformation conditions for achieving efficient power dissipation while avoiding flow instabilities.

2.3. Constitutive modeling

The flow stress of materials deformed at varying temperatures and strain rates can be predicted using constitutive modeling. The relationship between flow stress, temperature and strain rate can be described as follows [17]:

$$\dot{\varepsilon} = A[\sinh(\alpha\sigma)]^n \exp\left(-\frac{Q}{RT}\right) \tag{4}$$

Taking the natural logarithm of Eq. (4) yields:

$$\ln\dot{\varepsilon} = \ln A + n\ln[\sinh(\alpha\sigma)] - \frac{Q}{RT} \tag{5}$$

Here, *n* and *A* represent material constants, α denotes the stress multiplier, σ indicates the peak flow stress, *Q* stands for the activation energy for hot deformation, *R* is the universal gas constant, and *T* refers to the deformation temperature. The peak flow stress, σ_p is used as a proxy for σ, to represent the dynamic balance between work hardening and dynamic restoration. The stress multiplier α is defined as $\alpha = \beta/n_1$, where β and n_1 are derived from the slopes of the $\ln(\dot{\varepsilon})$ versus σ_p and $\ln(\dot{\varepsilon})$ versus $\ln(\sigma_p)$ plots, respectively, within the analyzed temperature range. The initial constitutive equation, when partially differentiated, indicates a constant activation energy independent of temperature and strain rate, expressed as $Q = RnS$. In this context, *n* denotes the mean slope of the $\ln(\dot{\varepsilon})$ vs $\ln[\sinh(\alpha\sigma_p)]$ graphs at different temperatures, whereas *S* represents the mean slope of the $\ln[\sinh(\alpha\sigma_p)]$ versus $1/T$ graphs at different strain rates. In addition, the value of *A* can be determined from the slope of the ln*Z* vs. $\ln[\sinh(\alpha\sigma_p)]$ plot. The constitutive equation for a specific strain can thus be derived by calculating the constants *n*, α, *A*, and *Q* and substituting them into Eq. (4).

3. Results and Discussion

3.1. Hot compressive behavior

The true stress-strain curves for X70 steel (Fig. 1) demonstrate a significant influence of temperature and strain rate on flow stress. Higher strain rate results in higher stress, while increasing temperature lowers stress. Three primary deformation patterns are observed: work

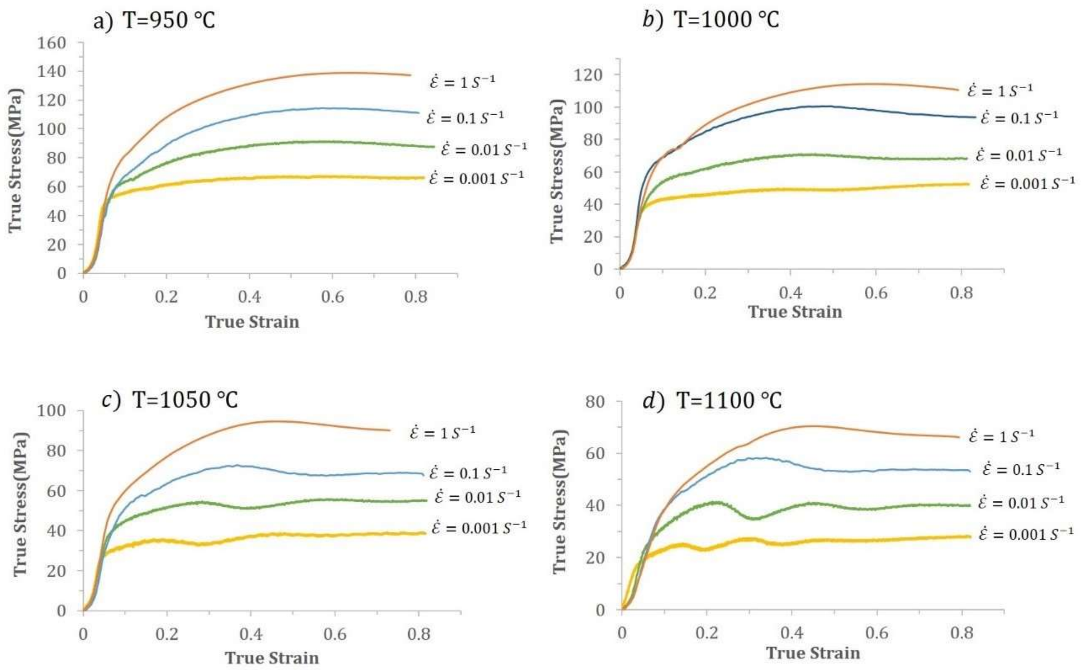

Fig. 1. Flow stress curves of API X70 steel obtained at various strain rates ranging from 0.001 s^{-1} to 1 s^{-1} and temperatures of (a) 950 ˚C, (b) 1000 ˚C, (c) 1050 ˚C, and (d) 1100 ˚C.

hardening, dynamic recovery (DRV), and dynamic recrystallization (DRX). At lower temperatures and higher strain rates, work hardening dominates, leading to a continuous increase in stress. At intermediate temperatures and strain rates, DRV mechanisms become more pronounced, resulting in stress plateaus or less pronounced peaks. At higher temperatures and lower strain rate, recrystallization becomes more prevalent, producing flow stress peaks.

The stress values reach their maximum at a strain rate of 1 s^{-1} and a temperature of 950 °C, while the minimum values are recorded at 0.001 s^{-1} and 1100 °C. At 950 °C, the flow curve indicates that work hardening and DRV balance each other, resulting in a near-saturation behavior rather than continuous hardening across the strain range. DRV is also prominent at 1000 °C and a strain rate of 1 s^{-1}. The appearance of stress peaks, particularly at higher temperatures (1050 and 1100 °C), suggests the occurrence of recrystallization. The stress-strain behavior shows a clear dependence on strain rate. At high strain rates (0.1 s^{-1} and 1 s^{-1}) the curves exhibit a broad single peak, while at lower strain rates (0.01 s^{-1} and 0.001 s^{-1}), multiple peaks and fluctuations are observed.

This transition from multiple- to single-peak behavior can be rationalized using the framework proposed by Sakai and Jonas [18], which considers the relative magnitudes of the peak strain (ε_p), the critical strain for DRX initiation (ε_c), and the strain for completion of softening (ε_x). At low strain rates, $\varepsilon_c < \varepsilon_x$, meaning that before the first recrystallization cycle completes, some regions of the material already reach the critical strain for a new nucleation events. As a result, several overlapping recrystallization cycles occur simultaneously, each at a different stage of evolution, leading to the multiple peaks and fluctuations observed in the flow curves. In contrast, at higher strain rates, $\varepsilon_c > \varepsilon_x$, and the nucleation of new grains is largely confined to ε_c, with grain growth completed by ε_x. Under these conditions, recrystallization follows a single softening cycle, resulting in a broad single peak in the flow curve.

3.2. Processing map

The processing maps were constructed using SigmaPlot software, generating three-dimensional (3D) curves (Fig. 2) and two-dimensional (2D) iso-efficiency maps (Fig. 3) to examine the relationship between temperature, strain rate, and power efficiency during compression tests at

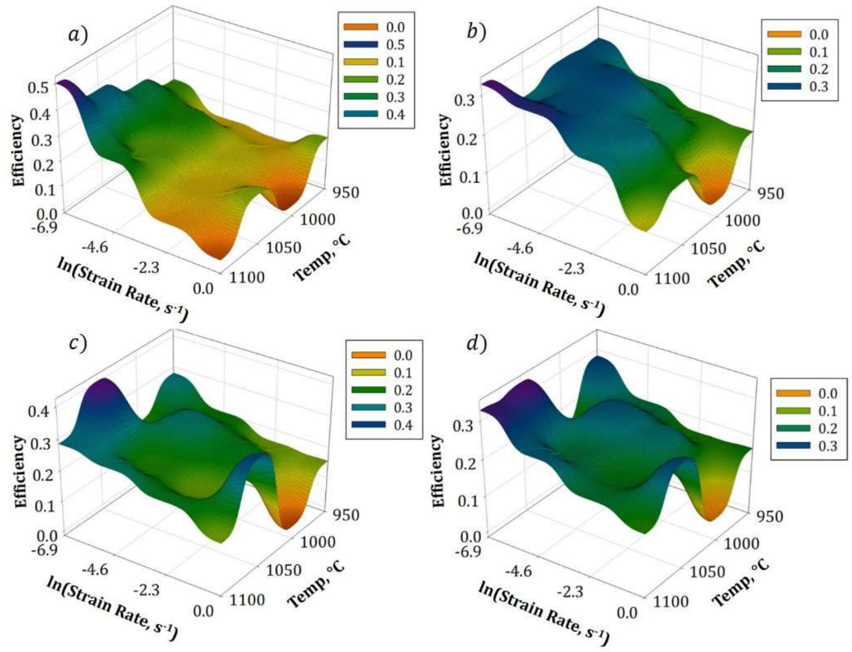

Fig. 2. 3D power efficiency maps for X70 steel corresponding to strain values of (a) 0.2, (b) 0.4, (c) 0.6, and (d) 0.7.

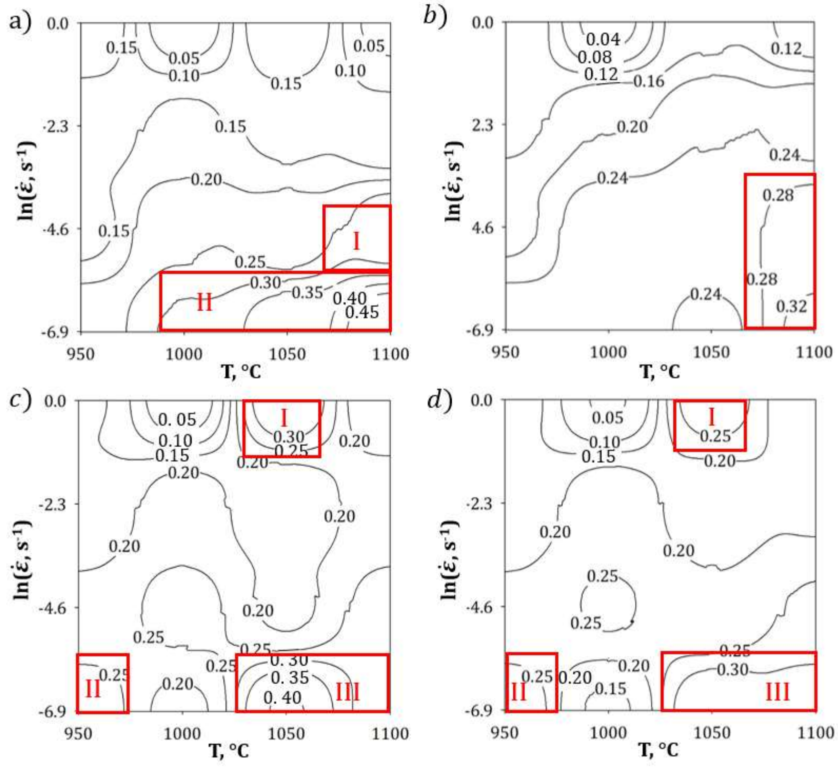

Fig. 3. The iso-efficiency contour map for X70 steel corresponding to strain values of (a) 0.2, (b) 0.4, (c) 0.6, and (d) 0.7.

various strains. The results indicate that lower temperatures and higher strain rates generally lead to lower efficiency values. Conversely, higher temperatures and lower strain rates result in higher efficiency.

The minimum efficiency for all four strains occurs at a temperature of 1000 °C and a strain rate of 1 s^{-1}. The highest efficiency, approximately 50%, is observed at a strain of 0.2, a temperature of 1100 °C, and a strain rate of 0.001 s^{-1}. It should be noted that the efficiency of power dissipation is derived from strain-rate sensitivity and can reach high values even before the flow curve attains its peak stress. Thus, the maximum efficiency observed at a strain of 0.2 does not indicate that peak stress has been reached under all deformation conditions. The maximum peak also occurs at the same temperature and strain rate, but with a lower value at larger strains. In addition to this maximal peak, two additional local maxima are observed. For instance, at 955 °C and a strain rate of 0.001 s^{-1}, an efficiency of 28% is recorded at a strain of 0.7, which may be attributed to DRV, as supported by the stress-strain curve data. Another peak, with an efficiency of 33%, is observed 1050 °C and a strain rate of 1 s^{-1}, associated with recrystallization. The peak efficiency windows vary with strain. At a strain of 0.2, two distinct windows are observed, whereas at a strain of 0.4, a single window is identified. For strains of 0.6 and 0.7, three peak efficiency specific windows are evident, highlighted as red rectangles in the 2D iso-efficiency maps.

The instability criterion values calculated for strains of 0.2, 0.4, 0.6, and 0.7 were fitted to a third-degree polynomial function, and the resulting contour plots were generated using SigmaPlot software (Fig. 4**)**. In general, the instability maps indicate that instability regions shrink as the strain increases. This trend is consistent with previous findings for 40MnBH alloy steel [19]. At lower deformation levels, work hardening dominates, leading to insufficient deformation driving forces and reduced formability. With increasing deformation, DRX softening gradually overcomes work hardening. At full DRX, most of the original work hardening is offset, resulting in improved processing performance and fewer instability regions.

For a strain of 0.2, the central region of the contour plot exhibits negative values, indicating instability. Stable regions are identified under the following conditions:1) 950 °C with strain rates of 1 and 0.1 s^{-1}; 2) 1050 and 1100 °C with a strain rate of 0.001 s^{-1}, and 3) at 1000 °C with a strain rate of 0.001 and 0.01 s^{-1}. At a strain of 0.4, the lower portion of the contour, corresponding to low strain rates, is predominantly stable, wheras high strain rate conditions are mostly unstable. The instability contours for strains of 0.6 and 0.7 are nearly identical, with minimal differences in the stable regions. A small region at a strain rate of 1 s^{-1} and a temperature of 1100 °C exhibits negative contour values at a strain of 0.6; however, this region becomes stable as the strain increases to 0.7. In contrast, conditions of 1000 °C and strain rates of 1 s^{-1} and 0.1 s^{-1} were unstable across all four strains, with low and near-zero efficiency. Microstructural analysis confirmed this prediction, revealing numerous cracks and voids at 1000 °C and a strain rate of 0.1 s^{-1}.

Processing maps were constructed by superimposing contours of constant efficiency and instability regions for strains for strains of 0.2, 0.4, 0.6, and 0.7 (Fig. 5). Unstable flow areas are marked in dark colors, while optimal hot deformation windows are indicated by red rectangles. Constant efficiency contours are also plotted within these regions. Table 2 summarizes the best stress and strain rate conditions for stable hot deformation across different strain levels. At strains of 0.2 and 0.4, a single stable zone is identified, but three optimal zones, approximately situated in the same locations on the maps, are identified at higher strains of 0.6 and 0.7. Overall, the maps show that unstable regions are more extensive at lower strains (0.2 and 0.4) than higher strains.

For strains up to 0.2, the optimal deformation conditions occur at a strain rate of 0.001 s^{-1} and a temperature of 1000 to 1100 °C, with predicted efficiencies exceeding 30%. At a strain of 0.4, stable regions with power efficiency between 28% to 32%

Table 2. Temperature and strain rate conditions for X70 steel corresponding tooptimal deformation at different strain levels

Strain	Area	Efficiency (%)	Temperature (°C)	Strain rate (s^{-1})
0.2	I	25 to 45	975-1100	0.001-0.005
0.4	I	28 to 32	1075-1100	0.001-0.05
0.6	I	25 to 33	1025-1075	0.5-1
	II	25 to 28	950-975	0.001-0.005
	III	26 to 28	1025-1100	0.001-0.005
0.7	I	25 to 27	1025-1075	0.5-1
	II	25 to 28	950-975	0.001-0.005
	III	25 to 33	1075-1100	0.001-0.005

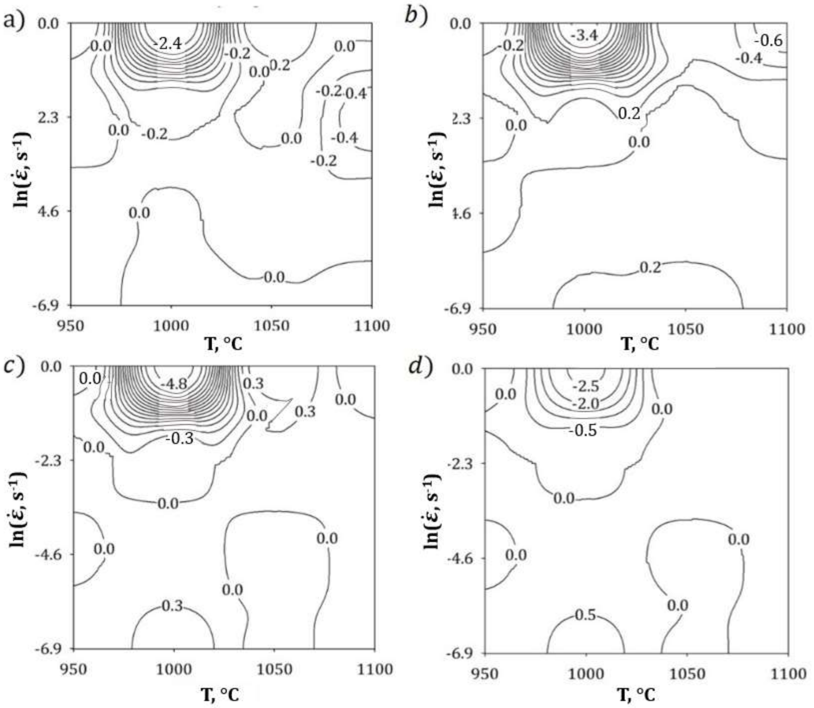

Fig. 4. Instability maps of X70 steel at different strain levels: (a) 0.2, (b) 0.4, (c) 0.6, and (d) 0.7.

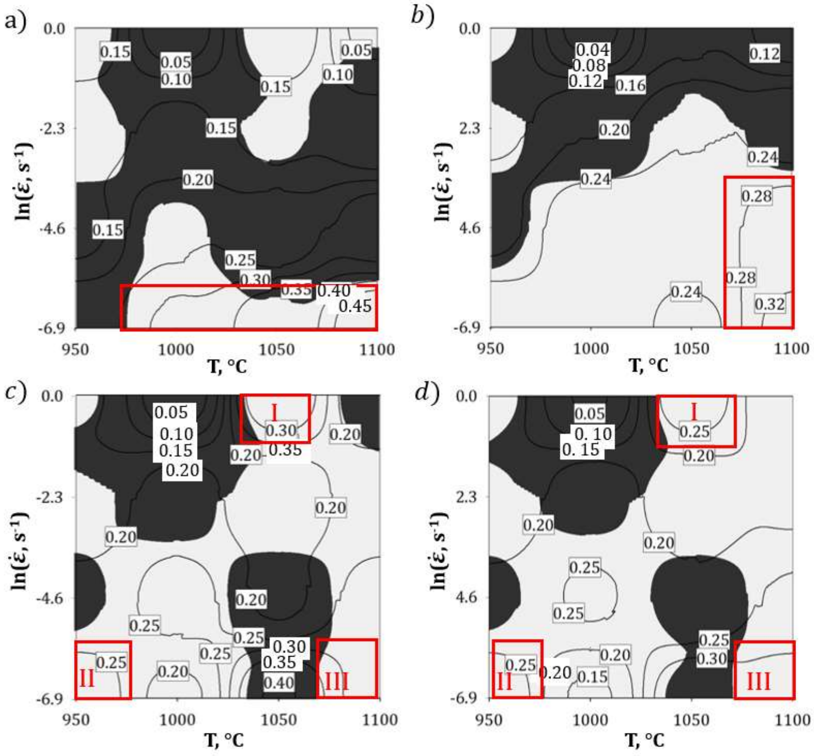

Fig. 5. Iso-efficiency processing maps of X70 steel for strain values of (a) 0.2, (b) 0.4, (c) 0.6, and (d) 0.7.

are found within a strain rate range of 0.001 s^{-1} to 0.05 s^{-1} and temperatures of 1075 °C-1100 °C. At lager strains (0.6 and 0.7), three optimal zones (Table 2, Fig. 5) can be identified. Among these, one region demonstrates the maximum efficiency. At a strain of 0.6, area I (1025-1075 °C, 0.5-1 s^{-1}) exhibits efficiency of 25% -33%. At a strain of 0.7, area III (1075-1100 °C, 0.001-0.005 s^{-1}), also is in the 25-33% range. For strains up to 0.7, safe deformation window at low strain rates (0.001 and 0.01 s^{-1}) exist at 950 °C - 975 °C (region II). Conversely, high strain rate (1 s^{-1}) deformation is recommended at 1025 °C to 1075 °C (region I).

It is worth noting that certain regions of the processing maps, particularly around 1050 °C at low strain rates, display relatively high-power dissipation efficiency (η) while still falling within instability domains. This apparent contradiction indicates that, although DRX may initiate under these conditions, it is insufficient to fully counteract localized damage mechanisms such as cavity formation, shear banding, or crack initiation. Therefore, high η values in these zones should not be interpreted as indicators of safe processing on their own. A combined interpretation of η contours, instability criteria, and microstructural validation is essential to reliably identify stable and unstable deformation conditions.

Poliak et al. [20] identified regions of complete and partial DRX for X70 steel utilizing the Zener-Hollomon parameter. Their analysis predicts complete DRX within a temperature range of 1075-1100 °C and a strain rate range of 0.001-0.005 s^{-1}, while partial DRX occurs at 950-975 °C and the same strain rate range of 0.001-0.005 s^{-1}. Region I (1025–1075 °C, 0.5–1 s^{-1}) exhibits relatively high efficiency (25–33%); here, DRV processes, including dislocation annihilation and subgrain formation, together with interactions between dislocations and microalloy precipitates (Nb, Ti, V), likely contribute to enhanced efficiency in the absence of full DRX. Region II (950–975 °C, 0.001–0.005 s^{-1}) corresponds to conditions favoring partial DRX, consistent with Poliak et al.'s [20] predictions, where nucleation is activated but grain growth remains incomplete, leading to moderate efficiency. Region III (1075–1100 °C, 0.001–0.005 s^{-1}) represents the most favorable conditions, with efficiency values of 25–33% and microstructural validation confirming complete DRX and grain refinement. Taken together, these three regions highlight that optimal hot deformation behavior can arise from different mechanisms, DRV in region I, partial DRX in region II, and full DRX in region III, emphasizing the importance of interpreting processing maps in conjunction with microstructural evidence.

3.3. Activation energy and constitutive equation

Fig. 6 illustrates the graphical methodology employed to determine the key material constants and the activation energy for hot deformation of API X70 steel. Each sub-figure corresponds to a specific plot derived from the experimental data: Fig. 6(a) depicts the relationship between $\ln(\dot{\varepsilon})$ and $\ln(\sigma_p)$ at various temperatures, from which the average value of n_1 (8.1052) is obtained. Fig. 6(b) shows the linear correlation between $\ln(\dot{\varepsilon})$ and σ_p, where the average slope provides the constant β (0.115261 MPa^{-1}). These two parameters were then used to calculate the average stress multiplier α, determined to be 0.014221 MPa^{-1}. Fig. 6(c) displays the plots of $\ln(\dot{\varepsilon})$ versus $\ln[\sinh(\alpha\sigma_p)]$ at different temperatures; the average slope of which yields the value of n (6.124089). Fig. 6(d) illustrates the relationship between $\ln[\sinh(\alpha\sigma_p)]$ and $1/T$ at various strain rates, and the average slope of these lines gives the constant S (11.2). Utilizing these determined values, the activation energy for hot deformation (Q) was calculated as 572.5 kJ/mol. Finally, from the intercept of the $\ln Z$ vs. $\ln[\sinh(\alpha\sigma_p)]$ plot, the value of $\ln A$ was determined to be 48.47. Based on these results, the constitutive equation of X70 steel at peak strain is expressed as Eq. (6):

$$\dot{\varepsilon} = e^{48.47}[\sinh(0.014221\sigma)]^{6.124089}\exp\left(-\frac{572500}{RT}\right) \tag{6}$$

Table 3 presents a comparative summary of the activation energy (Q) for hot deformation of API X70 steel obtained in this study alongside various other carbon and microalloyed steels reported in the literature. The activation energy for hot deformation of the API X70 steel in the present study was 572.5 kJ/mol, which is higher than the values reported for other API steels, such as API X80 (488.7 kJ/mol), API X70 in previous work (393 kJ/mol), and API X65 (330 kJ/mol), as shown in Table 3.

Table 3. Comparison of activation energy for hot deformation of API X70 steel and other C-steels

Steel type	Activation energy, Q (kJ/mol)	Temperature range (°C)	Strain rate range (s^{-1})	Reference source
API X70	572.5	950–1100	0.001–1	Present work
API X80	488.7	950–1100	0.001–1	[22]
API X70	393	900–1200	0.05–15	[23]
API X65	330	950–1150	0.01–1	[24]
AISI 304L stainless steel	392	900–1100	0.001–1	[21]
Medium carbon Microalloyed steel	394	850–1150	0.0001–3	[25]
17–4 PH stainless steel	423	900-1150	0.0001–10	[26]
Low-alloy steel	440	1000–1200	0.12–2.4	[27]
Structural steel	399			
Medium carbon steel	411			
Pearlitic steel	350			

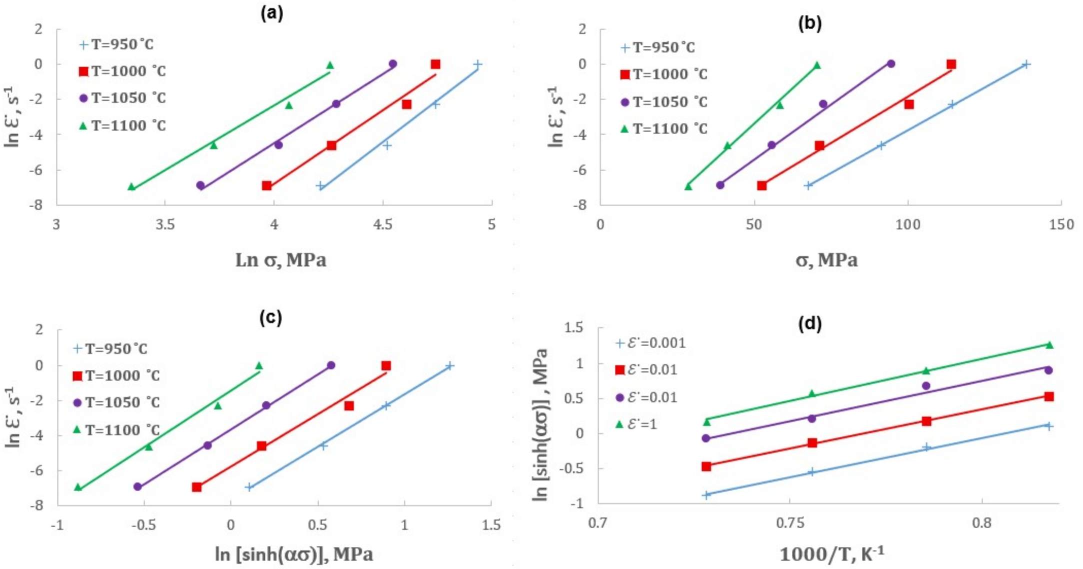

Fig. 6. Graphical determination of material constants and activation energy for API X70 steel: (a) $\ln(\dot{\varepsilon})$ vs. $\ln(\sigma_p)$ for determining n_1, (b) $\ln(\dot{\varepsilon})$ vs. σ_p for determining β, (c) $\ln(\dot{\varepsilon})$ vs. $\ln[\sinh(\alpha\sigma_p)]$ for determining n, and (d) $\ln[\sinh(\alpha\sigma_p)]$vs. 1/T for determining S.

The higher activation energy obtained in this study (~572.5 kJ/mol) compared to literature values can be attributed to factors such as grain size and texture. In particular, the combined effects of Nb, Ti, and V microalloying, along with the pinning effects of their precipitates on dislocations and grain boundaries, as well as differences in the initial microstructural condition play significant roles. These factors significantly influence the deformation resistance by affecting mechanisms such as dislocation motion and DRX. For instance, Mirzadeh et al. [21] reported a clear grain size dependence of activation energy in AISI 304L stainless steel, where the activation energy decreased from 393 to 363 kJ/mol as the grain size increased from 30 μm to 140 μm.

In addition to microstructural differences, the presence of microalloying elements such as Nb, Ti, and V in the current X70 steel likely plays a dominant role in increasing the activation energy. These elements form fine, stable precipitates that pin dislocations and grain boundaries, thereby impeding DRV and DRX processes. As a result, a higher energy barrier must be overcome for plastic deformation. Compared to non-microalloyed steels or those with lower alloying levels, such as medium carbon microalloyed steels (394 kJ/mol), stainless steels like 17–4 PH (423 kJ/mol), or other steels (350–440 kJ/mol), the activation energy determined in the present work further underscores the significant strengthening effect imparted by these microalloying additions. Therefore, the elevated activation energy reflects not only the processing conditions but also the alloy's strong resistance to hot deformation, highlighting the need for careful control of thermomechanical parameters during industrial processing.

3.4. Microstructural characterization

The microstructure of X70 steel was studied before and after homogenization at 1200 °C for 10 minutes followed by water quenching (Fig. 7).

The as-received condition showed a ferrite-pearlite morphology, with ferrite as a continuous matrix and pearlite as discrete colonies. This suggests prior heat treatment aimed at refining the microstructure and improving mechanical properties. Homogenization treatment produced significant transformation, potentially introducing additional phases like bainite, martensite, or retained austenite. Bainite forms during intermediate cooling rates between pearlite and martensite, while martensite forms upon rapid cooling. Retained austenite, the residual austenite untransformed after quenching, can influence the steel's mechanical properties.

The microstructure of X70 steel after hot compression at 1100 °C to a strain of 0.7 is depicted in Fig. 8 across a strain rate range of 0.001 s^{-1} to 1 s^{-1}. The results demonstrate a correlation between microstructure and strain rate. At lower strain rates, a relatively coarse-grained microstructure with more visible retained austenite grain boundaries was observed. With the increase in strain rate, DRX became more pronounced, resulting in progressive refinement of the microstructure and partial elimination of retained austenite grain boundaries.

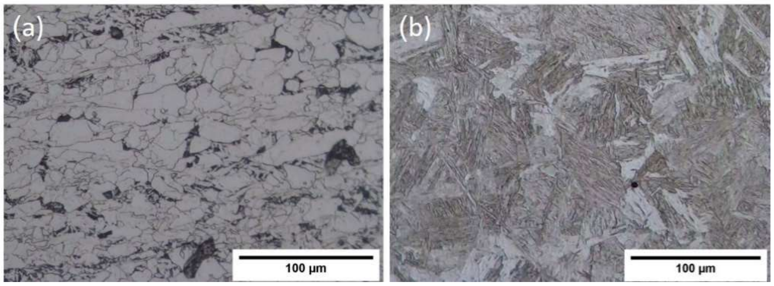

Fig. 7. Optical microstructures of X70 steel: (a) in the as-received condition; and (b) homogenized at 1200 °C for 10 minutes and subsequently quenched in water.

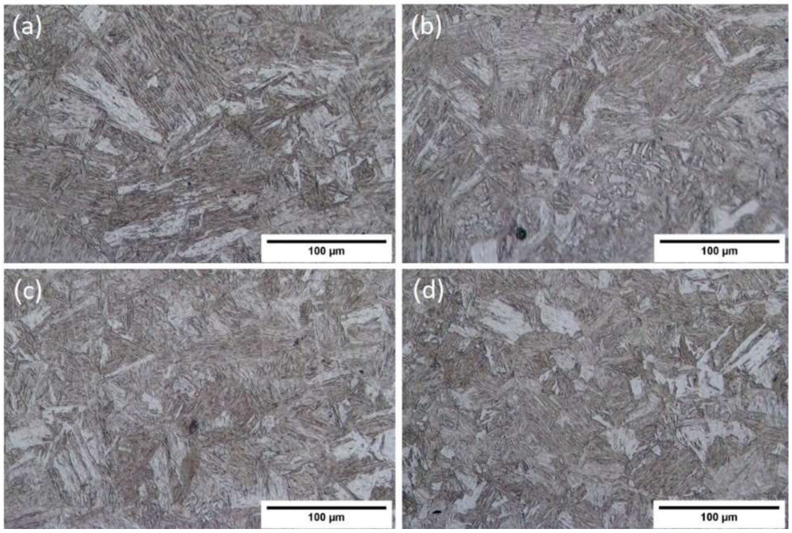

Fig. 8. Optical microstructure (revealed by Nital2% etching) of X70 steel deformed at a temperature of 1100 °C and strain rates of (a) 0.001, (b) 0.01, (c) 0.1, and (d) 1 s^{-1}. The micrographs were taken perpendicular to the compression axis.

The observed microstructural changes are consistent with the predictions of the processing map for X70 steel at 1100 °C and a strain of 0.7. The map indicates that deformation at this temperature is safe across a range of strain rates, suggesting that the observed microstructural evolution falls within the expected regime of stable processing conditions.

Fig. 9 presents the optical microstructures of X70 steel deformed at 1100 °C under various strain rates, obtained using Picral etching to reveal the prior austenite grain boundaries and illustrate the DRX mechanism. Notably, the grains are not well visible at lower strain rates (Fig. 9(a) and 9(b), corresponding to 0.001 s^{-1} and 0.01 s^{-1}, respectively). However, as the strain rate increases to 0.1 s^{-1} (Fig. 9(c)) and 1 s^{-1} (Fig. 9(d)), the grains become more distinct and visible due to the more pronounced occurrence of DRX. These microstructural observations, corresponding to conditions falling within or near the stable and optimized zones identified by the processing maps, provide crucial experimental validation, confirming that deformation in these regions promotes favorable microstructural evolution characterized by DRX and desirable grain characteristics. Based on the microstructure analysis and corresponding processing maps, the deformation conditions at 1000 °C and strain rates of 0.1 s^{-1} and 1 s^{-1} after a strain of 0.7 are of particular concern. In this regime, the processing map predicts near-zero deformation efficiency and unstable deformation behavior, which is corroborated by microstructural observations. Samples compressed at 1000 °C and a strain rate of 0.1 s^{-1} exhibited cavities and cracks (Fig. 10(a)). These defects indicate localized deformation and potential material failure. The cracks in Fig. 10(a) are attributed mainly to flow instability, as their alignment with deformation bands and absence in stable samples indicate a deformation-induced origin. Although martensitic transformation during quenching may contribute to cracking in some steels, it is considered a secondary effect under the present conditions.

Similarly, samples deformed at a strain rate of 1 s^{-1} showed evidence of deformation bands within the grains (Fig. 10(b)), suggesting a concentration of plastic deformation in specific regions. While no distinct cracks were observed at this condition, the presence of deformation bands indicates a precursor to localized deformation and potential instabilities. Another unstable region in the map with a strain of 0.7 corresponds to a temperature of 950 °C and a strain rate of 0.01 s^{-1}. No indications of instability were detected in this sample; however, in a similarly examined sample with a strain rate of 0.001 s^{-1}, localized flow was noted (Fig. 10(c)). These findings suggest that microstructural instability can occur not only within the predicted unstable domain but also in adjacent regions. Therefore, caution should be exercised when selecting deformation conditions near or within these areas to avoid unexpected material behavior.

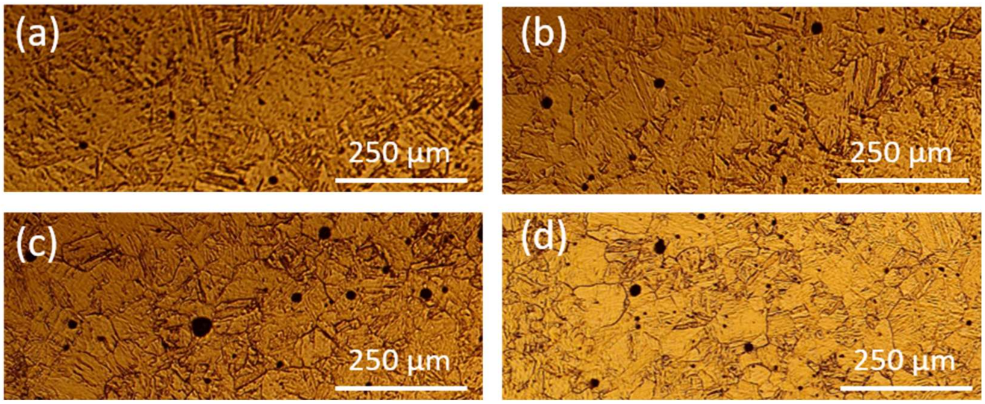

Fig. 9. Optical microstructures of API X70 steel deformed at 1100 °C, revealed by Picral etching to expose prior austenite grain boundaries, at initial strain rates of (a) 0.001 s^{-1}, (b) 0.01 s^{-1}, (c) 0.1 s^{-1}, and (d) 1 s^{-1}. The micrographs were taken perpendicular to the compression axis.

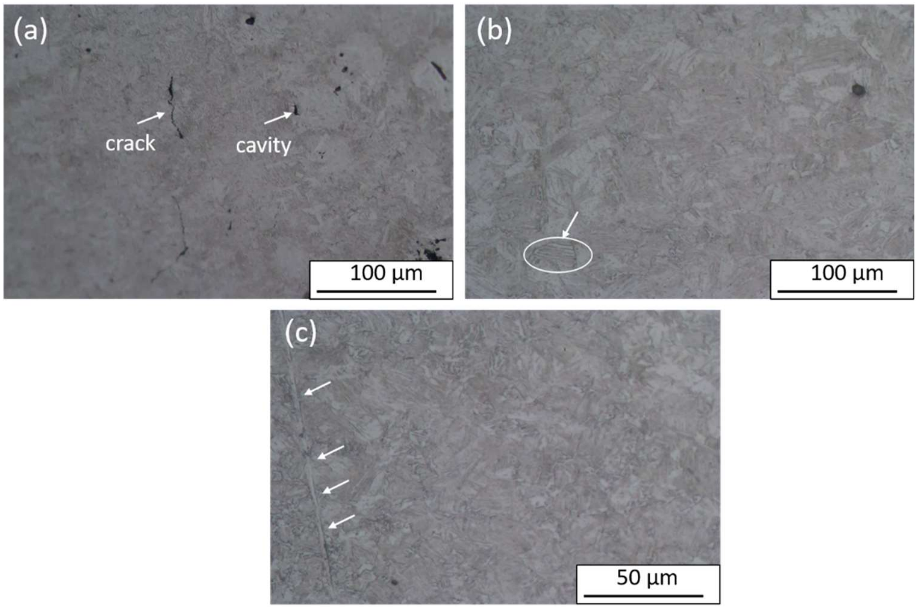

Fig. 10. The microstructure of X70 steel subjected to compression at 1000 °C with strain rates of (a) 0.1 s^{-1} and (b) 1 s^{-1} after a strain of 0.7. (c) The microstructure of X70 steel subjected to compression at 950 °C with strain rates of 0.001 s^{-1} after a strain of 0.7. The micrographs were taken perpendicular to the compression axis.

4. Conclusions

This study presents a comprehensive investigation of the hot deformation behavior of API X70 microalloyed steel through processing maps, constitutive modeling, and microstructural validation. The main findings are as follows:

1. The flow behavior was strongly influenced by temperature and strain rate. Higher strain rates promoted work hardening, while lower strain rates and higher temperatures facilitated DRV and DRX.
2. Processing maps constructed using power dissipation efficiency and instability criteria effectively identified between safe and unsafe deformation conditions. At higher strains (0.6–0.7), three optimal hot deformation zones were identified, with the most favorable located at 1075–1100 °C and 0.001–0.005 s^{-1} (efficiency: 25–33%).
3. Microstructural observations confirmed the reliability of the processing maps. Stable zones corresponded to fine recrystallized structures, while unstable regions showed cavities, deformation bands, or crack formation, particularly at 1000 °C and high strain rates.
4. The activation energy for hot deformation was calculated as 572.5 kJ/mol, which is higher than values reported for similar and other carbon steels. This elevated energy is attributed to differences in initial microstructure and chemical composition.

Authors' contributions

F. Ahmadi: Investigation, Formal analysis, Software

M. Reihanian: Conceptualization, Writing original draft, Writing-review and editing

M. Eskandari: Supervision

S. R. Alvai Zaree: Supervision

Conflict of interest

The authors have no relevant financial or non-financial interests to disclose.

Funding

The founding of Shahid Chamran University of Ahvaz through grant number SCU.EM1402.236 is gratefully appreciated.

5. References

[1] Villalobos, J. C., Del-Pozo, A., Campillo, B., Mayen, J., & Serna, S. (2018). Microalloyed steels through history until 2018: Review of chemical composition, processing and hydrogen service. *Metals*, *8*(5), 351. https://doi.org/10.3390/met8050351

[2] Vervynckt, S., Verbeken, K., Lopez, B., & Jonas, J. (2012). Modern HSLA steels and role of non-recrystallisation temperature. *International Materials Reviews*, *57*(4), 187-207. https://doi.org/10.1179/1743280411Y.0000000013

[3] Baker, T. N. (2016). Microalloyed steels. *Ironmaking & Steelmaking*, *43*(4), 264-307. https://doi.org/10.1179/1743281215Y.0000000063

[4] e Silva, A. C. (2020). Challenges and opportunities in thermodynamic and kinetic modeling microalloyed HSLA steels using computational thermodynamics. *Calphad*, *68*, 101720. https://doi.org/10.1016/j.calphad.2019.101720

[5] Masoumi, M., Herculano, L. F. G., & de Abreu, H. F. G. (2015). Study of texture and microstructure evaluation of steel API 5L X70 under various thermomechanical cycles. *Materials Science and Engineering: A*, *639*, 550-558. https://doi.org/10.1016/j.msea.2015.05.020

[6] Nafisi, S., Arafin, M., Collins, L., & Szpunar, J. (2012). Texture and mechanical properties of API X100 steel manufactured under various thermomechanical cycles. *Materials Science and Engineering: A*, *531*, 2-11. https://doi.org/10.1016/j.msea.2011.09.072

[7] Zidelmel, S., Rayane, K., & Kaouka, A. (2024). Effects of thermo-mechanical parameters on microstructural and mechanical properties of API X70 steel. *JOM, 76*, 3354-3361. https://doi.org/10.1007/s11837-023-06333-0

[8] Al Shahrani, A., Yazdipour, N., Dehghan-Manshadi, A., Gazder, A. A., Cayron, C., & Pereloma, E. V. (2013). The effect of processing parameters on the dynamic recrystallisation behaviour of API-X70 pipeline steel. *Materials Science and Engineering: A*, *570*, 70-81. https://doi.org/10.1016/j.msea.2013.01.066

[9] Mirzakhani, B., Salehi, M. T., Khoddam, S., Seyedein, S. H., & Aboutalebi, M. R. (2009). Investigation of dynamic and static recrystallization behavior during thermomechanical processing in a API-X70 microalloyed steel. *Journal of Materials Engineering and Performance*, *18*, 1029-1034. https://doi.org/10.1007/s11665-008-9338-x

[10] Prasad, Y. V. R. K. (2003). Processing maps: A status report. *Journal of Materials Engineering and Performance*, *12*(6), 638-645. https://doi.org/10.1361/105994903322692420

[11] Prasad, Y. V. R. K., & Seshacharyulu, T. (1998). Modelling of hot deformation for microstructural control. *International Materials Reviews*, *43*(6), 243-258. https://doi.org/10.1179/imr.1998.43.6.243

[12] Eskandari, H., Reihanian, M., & Alavi Zaree, S. (2023). An Analysis of Efficiency Parameter and its Modifications Utilized for Development of Processing Maps. *Iranian Journal of Materials Forming*, *10*(4), 45-51. https://doi.org/10.22099/ijmf.2024.49537.1283

[13] Prasad, Y. V. R. K., Gegel, H. L., Doraivelu, S. M., Malas, J. C., Morgan, J. T., Lark, K. A., & Barker, D. R. (1984). Modeling of dynamic material behavior in hot deformation: Forging of Ti-6242. *Metallurgical Transactions A*, *15*(10), 1883-1892. https://doi.org/10.1007/BF02664902

[14] Zhou, G., Ding, H., Cao, F., & Zhang, B. (2014). A comparative study of various flow instability criteria in processing map of superalloy GH4742. *Journal of Materials Science & Technology*, *30*(3), 217-222. https://doi.org/10.1016/j.jmst.2013.07.008

[15] Ebrahimi, R., & Najafizadeh, A. (2004). Optimization of hot workability in Ti-IF steel by using the processing map. *International Journal of ISSI*, *1*(1), 1-7. https://journal.issiran.com/article_4653.html

[16] Murty, S. V. S. N., & Rao, B. N. (1998). On the development of instability criteria during hotworking with reference to IN 718. *Materials Science and Engineering: A*, *254*(1), 76-82. https://doi.org/10.1016/S0921-5093(98)00764-3

[17] Sellars, C. M., & McTegart, W. J. (1966). On the mechanism of hot deformation. *Acta Metallurgica*, *14*(9), 1136-1138. https://doi.org/10.1016/0001-6160(66)90207-0

[18] Sakai, T., & Jonas, J. J. (1984). Overview no. 35 dynamic recrystallization: mechanical and microstructural considerations. *Acta metallurgica*, *32*(2), 189-209. https://doi.org/10.1016/0001-6160(84)90049-X

[19] Chai, R. X., Zhang, C. W., Guo, W., & Zhang, F. (2017). Hot deformation behavior and processing map of 40MnBH alloy steel. *Steel Research International*, *88*(5), 1600281. https://doi.org/10.1002/srin.201600281

[20] Poliak, E. I. (2020). Dynamic recrystallization control in hot rolling. *Procedia Manufacturing*, *50*, 362-367. https://doi.org/10.1016/j.promfg.2020.08.067

[21] Mirzadeh, H., Parsa, M., & Ohadi, D. (2013). Hot deformation behavior of austenitic stainless steel for a wide range of initial grain size. *Materials Science and Engineering: A*, *569*, 54-60. https://doi.org/10.1016/j.msea.2013.01.050

[22] Eskandari, H., Reihanian, M., & Zaree, S. A. (2024). Constitutive modeling, processing map optimization, and recrystallization kinetics of high-grade X80 pipeline steel. *Journal of Materials Research and Technology*, *33*, 2315-2330. https://doi.org/10.1016/j.jmrt.2024.09.217

[23] Xu, Y., Tang, D., Song, Y., & Pan, X. (2012). Dynamic recrystallization kinetics model of X70 pipeline steel. *Materials & Design*, *39*, 168-174. https://doi.org/10.1016/j.matdes.2012.02.034

[24] Rakhshkhorshid, M., & Hashemi, S. (2013). Experimental study of hot deformation behavior in API X65 steel. *Materials Science and Engineering: A*, *573*, 37-44. https://doi.org/10.1016/j.msea.2013.02.045

[25] Mirzadeh, H., Cabrera, J., Prado, J., & Najafizadeh, A. (2011). Hot deformation behavior of a medium carbon microalloyed steel. *Materials Science and Engineering: A*, *528*(10-11), 3876-3882. https://doi.org/10.1016/j.msea.2011.01.098

[26] Mirzadeh, H., Cabrera, J. M., & Najafizadeh, A. (2011). Constitutive relationships for hot deformation of austenite. *Acta Materialia*, *59*(16), 6441-6448. https://doi.org/10.1016/j.actamat.2011.07.008

[27] Menapace, C., Sartori, N., Pellizzari, M., & Straffelini, G. (2018). Hot deformation behavior of four steels: a comparative study. *Journal of Engineering Materials and Technology*, *140*(2), 021006. https://doi.org/10.1115/1.4038670